Ab initio study of the stability and elasticity of brucite

Hongjin Wang,[1] Chenxing Luo,[1] and Renata M. Wentzcovitch[1,2,3,4,*]
[1]*Department of Applied Physics and Applied Mathematics, Columbia University, New York, New York 10027, USA*
[2]*Department of Earth and Environmental Sciences, Columbia University, New York, New York 10027, USA*
[3]*Lamont–Doherty Earth Observatory, Columbia University, Palisades, New York 10964, USA*
[4]*Data Science Institute, Columbia University, New York, New York 10027, USA*

(Received 21 November 2023; revised 27 April 2024; accepted 20 May 2024; published 4 June 2024)

Brucite [$Mg(OH)_2$] is a mineral of great interest owing to its various applications and roles in geological processes. Its structure, behavior under different conditions, and unique properties have been the subject of numerous studies and persistent debate. As a stable hydrous phase in subduction zones, its elastic anisotropy can significantly contribute to the seismological properties of these regions. We performed *ab initio* calculations to investigate brucite's stability, elasticity, and acoustic velocities. We tested several exchange-correlation functionals and managed to obtain stable phonons for the $P\bar{3}$ phase with r^2SCAN at all relevant pressures up to the mantle transition zone. We show that r^2SCAN performs very well in brucite, reproducing the experimental equation of state and several key structure parameters related to hydrogen positions. The room-temperature elasticity results in $P\bar{3}$ reproduces the experimental results at ambient pressure. These results, together with the stable phonon dispersion of $P\bar{3}$ at all relevant pressures, indicate $P\bar{3}$ is the stable candidate phase not only at elevated pressures but also at ambient conditions. The success of r^2SCAN in brucite suggests this functional should be suitable for other challenging layer-structured minerals, e.g., serpentines, of great geophysical significance.

DOI: 10.1103/PhysRevB.109.214103

I. INTRODUCTION

Water, incorporated stoichiometrically in hydrous minerals, as hydrous defects, or in melts, plays a pivotal role in Earth's interior dynamics. It lowers the subsolidus viscosity of rocks and internal frictions facilitating earthquakes [1,2]. Each year, significant amounts of water ($\sim 10^{11}$ kg) enter Earth's mantle through the subduction process [3]. In the upper mantle, water reacts with rocks beneath the crust to form hydrous minerals and enters the subduction process. Carried to greater depths, increased pressure and temperature produce dehydration, resulting in slab embrittlement. Formed at the early stages of the subduction process, sheetlike hydrous minerals, e.g., brucite and serpentine phases, are the major water carriers at upper mantle depths. These minerals consist of Mg-Si-O–containing layers bounded only by hydrogen bonds (H bonds) and are weak in shear strengths, facilitating the slab subduction process [4,5]. Given the intricate details of their formation and participation in geotectonic processes, the understanding of serpentine phases deepens our grasp of geological processes in the upper mantle and the importance of water in shaping them.

To address phase relations in these hydrous phases, it is necessary to address brucite ($Mg(OH)_2$) first. As one of the simplest and most water-abundant minerals within the ternary $MgO-SiO_2$-H_2O (MSH) system [6], brucite is central in the many geochemical processes of serpentine formation and transformation that occur in subducted slabs. For example, brucite participates in the retrograde formation of antigorite from olivine (Mg_2SiO_4) or dehydration of antigorite ($Mg_{3m-3}Si_{2m}O_{5m}(OH)_{4m-6}$) [4] and in the lizardite ($Mg_3Si_2O_5(OH)_4$) to antigorite transition [4,7,8], both being serpentine-type phases. So we need to address brucite also to understand phase relations between these complex serpentine phases.

Ever since the structure of brucite was first refined in 1967 with the space group $P\bar{3}m1$ [9], such assignment has been a subject of continuous debate. The original work did not account for the "riding" motion of hydrogen and got an inaccurate O—H bond length [10]. Neutron diffraction [11,12] and *ab initio* molecular dynamics simulations [13] suggest protons are displaced from the threefold axis at elevated pressures. To accommodate this disordered displacement of protons from high-symmetry positions, an enlarged $\sqrt{3} \times \sqrt{3} \times 1$ supercell structure with lower $P\bar{3}$ symmetry was proposed in 2006 [14]. Still, no consensus has been reached on whether $P\bar{3}m1$, [15,16] or $P\bar{3}$ [17], or a structure with even lower symmetry [18] describes brucite's stable phase at ambient conditions.

Resolving the structure of brucite and being able to describe its vibrational properties is the first step to computing its thermodynamic and thermoelastic properties at high pressures and high temperatures (high-PT). The Wu-Wentzcovitch semianalytical method (SAM-Cij) [19,20] is a concise and predictive formalism to calculate the thermoelastic tensor (Cij) of crystalline solids that depends on the existence of stable phonons [21–23], still debatable for brucite minerals [15,18]. This method has been successfully applied to materials across all crystal systems in conjunction with

---

[*] rmw2150@columbia.edu

ab initio calculations of static elastic coefficients and phonon frequencies.

This work reevaluates brucite's phonon stability issue using density-functional theory (DFT) with an r^2SCAN [24] description of the exchange-correlation energy. Compared to Perdew-Burke-Ernzerhof (PBE) formula [25] and the local density approximation (LDA) [26], the SCAN meta–generalize gradient approximation (GGA) functionals [27] better describe the H-bond compressive behavior [28–31]. The r^2SCAN functional has the same accuracy as the SCAN functional but performs better numerically [24]. It also slightly improves dynamic stability [32,33]. This method stabilizes the $P\bar{3}$ structure's phonon dispersion in a wide pressure range of geophysical significance. Here we report the high-temperature elastic properties and velocities of brucite using the SAM-Cij method.

This paper is organized as follows. Section II introduces the method and DFT calculation parameters. We show results and compare them with measurements and previous calculations in Sec. III. Summary and conclusions are presented in Sec. IV.

II. METHOD

All density-functional-theory calculations were conducted using the projector augmented wave (PAW) method [34] implemented in the VASP code [35]. We employed the r^2SCAN [24] exchange-correlation functional. LDAs [26] and GGAs parameterized by PBE [25] were also used to compare with the r^2SCAN results. A plane-wave basis was used with a kinetic energy cutoff of 800 eV. We chose a k-point mesh of $4 \times 4 \times 4$ which ensures the convergence of 1 meV/atom. The convergence criteria were 10^{-5} eV for the total energy and 10^{-3} eV/Å for the atomic force. For phonon calculation, the convergence criterion was 10^{-8} eV for the total energy. The full Brillouin zone phonon spectra were calculated on the $2 \times 2 \times 2$ supercells using the finite-displacement method implemented in PHONOPY [36]. For Fig. 2, PREC = accurate, ENCUT = 800 eV are chosen in VASP calculations, and the finite displacement is set to 0.02 Å in PHONOPY. A comparison of phonon dispersions calculated with r^{2}SCAN and SCAN using various finite displacement values and fast-Fourier-transform grid density parameters is shown in Fig. S1 [37]. The structures at elevated pressures are calculated by uniformly scaling the structure at ambient pressure and then relaxing at constant volumes. The static elastic coefficient tensor was obtained using the stress vs strain relations resulting from ±1% infinitesimal strain.

The high-temperature elastic tensor is calculated using the PYTHON package `cij` [20]. Its components are written as a derivative of the Helmholtz free energy under isothermal conditions [19,20,38]:

$$c_{ijkl}^{T} = \frac{1}{V}\left(\frac{\partial^2 F}{\partial e_{ij}\partial e_{kl}}\right) + \frac{1}{2}P(2\delta_{ij}\delta_{kl} - \delta_{il}\delta_{kj} - \delta_{ik}\delta_{jl}). \quad (1)$$

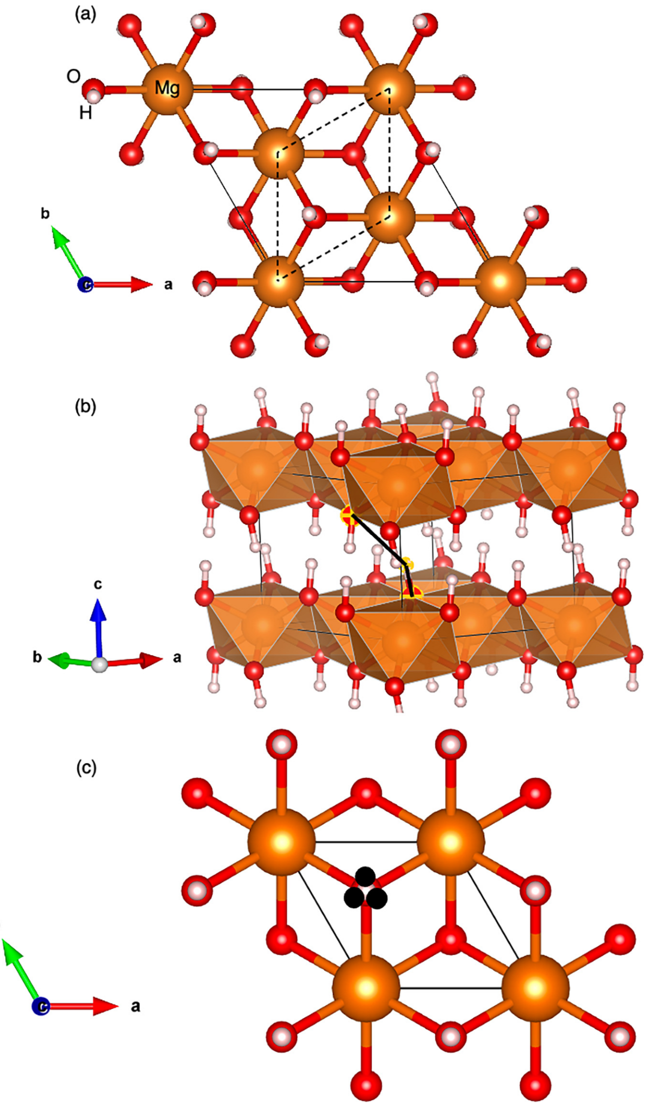

FIG. 1. Crystal structure of brucite: (a) Top view of the unit cell of a $P\bar{3}$ brucite with lattice vectors shown as solid black lines. The lattice vectors of the smaller and more symmetric $P\bar{3}m1$ structure are shown as dashed lines. (b) Side view of a $P\bar{3}$ brucite. Highlighted atoms show a typical interlayer H bond (bold solid lines). Yellow: Mg; red: O; white: H. (c) Illustration of $2d$ and $6i$ site in the $P\bar{3}m1$ brucite. The original hydrogen atoms sit at the $2d$ site. The three black circles above the oxygen atom are hydrogen atoms at the $6i$ site. There are also three circles below the other oxygen atom in the unit cell.

Here, e_{ij}, e_{kl} $(i, j, k, l = 1, 2, 3)$ represents the infinitesimal strains, P represents pressure, δ_{ij} represents the Kronecker delta symbol, and F represents the Helmholtz free energy, which can be calculated as follows using the quasiharmonic approximation (QHA) [39]:

$$F(e_{ij}, V, T) = U(e_{ij}, V) + \frac{1}{2}\sum_{q,m}\hbar\omega_{q,m}(e_{ij}, V) + k_B T \sum_{q,m} \ln\left\{1 - \exp\left[-\frac{\hbar\omega_{q,m}(e_{ij}, V)}{k_B T}\right]\right\}. \quad (2)$$

Here, $\omega_{q,m}$ represents the vibrational frequency of the mth normal mode with the phonon wave vector q. V, T represent

TABLE I. Calculated structure parameters compared to previous measurements at ambient conditions and static calculation results at 0 GPa, unless otherwise stated.

Space group[a]	a (Å)	c (Å)	c/a	Volume (Å^3)	Method	Reference
$P\bar{3}m1$	3.146	4.768	1.515	40.868	X-ray diffraction	Fei and Mao (1993) [43]
$P\bar{3}m1$	3.138	4.713	1.502	40.200	Neutron diffraction	Parise (1994) [12]
$P\bar{3}m1$	3.150	4.720	1.498	40.560	Neutron diffraction	Catti (1995) [11]
$P\bar{3}m1$	3.145	4.769	1.516	40.851	X-ray diffraction	Duffy (1995) [44]
$P\bar{3}m1$	3.148	4.779	1.518	41.015	Neutron diffraction	Desgranges (1996) [41]
$P\bar{3}m1$	3.148	4.771	1.516	40.930	X-ray diffraction	Fukui (2003) [45]
$P\bar{3}m1$	3.150	4.783	1.518	41.101	Brillouin scattering	Jiang (2006) [46]
$P\bar{3}m1$	3.155	4.772	1.512	41.147	Neutron diffraction	Xu (2013) [47]
$P\bar{3}m1$	3.147	4.757	1.512	40.793	X-ray diffraction	Ma (2013) [48]
$P\bar{3}m1$	3.146	4.770	1.516	40.890	X-ray diffraction	Pillai (2021) [15]
$P\bar{3}$	3.199	4.844	1.514	41.780	PBE	Mookherjee and Stixrude (2006) [14]
$P\bar{3}$	3.070	4.400	1.433	36.000	LDA	Ghaderi (2015) [7]
$P\bar{3}$	3.080	4.440	1.442	36.660	LDA+MGD 300 K	Ghaderi (2015) [7]
$P\bar{3}$	3.200	4.840	1.513	41.700	PBE	Ghaderi (2015) [7]
$P\bar{3}m1$	3.188	4.786	1.501	42.120	PBEsol	Treviño (2018) [18]
$P\bar{3}$	3.186	4.777	1.499	42.000	PBEsol	Treviño (2018) [18]
$P\bar{3}m1$	3.141	4.666	1.486	39.900	B3LYP-D	Ulian (2019) [49]
$P\bar{3}$	3.129	4.657	1.488	39.500	B3LYP-D	Ulian (2019) [49]
$P\bar{3}m1$	3.186	4.848	1.522	42.611	vdW-DF2	Pillai (2021) [15]
$P\bar{3}m1$	3.088	4.406	1.427	36.390	LDA	This work
$P\bar{3}$	3.071	4.399	1.432	35.932	LDA	This work
$P\bar{3}m1$	3.181	4.795	1.507	42.035	PBE	This work
$P\bar{3}$	3.179	4.789	1.506	41.923	PBE	This work
$P\bar{3}m1$	3.137	4.633	1.477	39.470	r^2SCAN	This work
$P\bar{3}$	3.128	4.645	1.485	39.347	r^2SCAN	This work

[a] We keep the original convention from the references.

the equilibrium volume and temperature. $\hbar$ and k_B are the reduced Planck and Boltzmann constant, respectively.

Crystal structure images are created using VESTA [40].

III. RESULTS AND DISCUSSION

A. Structure optimization

The crystal structure of brucite was first refined by Zigan and Rothbauer [9] in the space group $P\bar{3}m1$ with protons on the threefold axis corresponding to the $2d$ Wyckoff position $(1/3, 2/3, z)$. Each hydroxyl is surrounded by three oppositely oriented hydroxyl groups of the overlying layer. Subsequent theoretical [13] and experimental studies [41] found the protons tend to displace from the $2d$ site to the $6i$ Wyckoff site at $(x, 2x, z)$ with an occupation of $1/3$ at elevated pressure. The value of x could be either $>1/3$ (the so-called x greater than third, or XGT, arrangement) or $<1/3$ (the x less than third, or XLT, arrangement). In *ab initio* calculations, the $1/3$ occupation can be simulated by supercells. Mookherjee and Stixrude [14] modeled the transition of hydrogen to XGT position using an enlarged $\sqrt{3} \times \sqrt{3} \times 1$ supercell. This model minimizes the interlayer H $\cdots$ O distance, resulting in a $P\bar{3}$ symmetry (a maximum subgroup of $P\bar{3}m1$) for brucite. The XLT arrangement conserves the $P\bar{3}m1$ symmetry but is energetically unfavorable. It is important to note that the $P\bar{3}$ model is equivalent to $P\bar{3}m1$ with displaced hydrogen at the $6i$ position. The relation of $P\bar{3}$ and $P\bar{3}m1$ brucite is shown in Fig. 1.

Table I shows the lattice parameters and volumes at ambient conditions compared to the previous calculations and measurements. In $P\bar{3}$, a is divided by $\sqrt{3}$ for comparison with $P\bar{3}m1$. All experiments in Table I are at room temperature and ambient pressure, and all calculations are static 0 GPa unless otherwise stated. It is also important to notice that even though all experiments assume the space group of $P\bar{3}m1$, some did obtain the results where hydrogen atoms are favored at $6i$ positions [11,12,41]. The most important factor for all calculations is the choice of exchange-correlation functionals. Our results are similar to previous results with the same exchange-correlation functionals. The $P\bar{3}$ brucite is slightly smaller than the $P\bar{3}m1$ counterpart. The difference between the two phases also depends heavily on the choice of exchange-correlation functionals. For PBE or PBEsol functionals, the difference is minor, at 0.001 Å for a and 0.01 Å for c. Our LDA results show a difference of 0.02 Å in a and 0.1 Å in c. Also, since all measurements are performed at room temperature, an ideal description of static volume needs to be smaller than the measurements (volume $<$41 Å^3). In Table I, only LDA, B3LYP-D, and r^2SCAN satisfy this condition. In addition, Ref. [7] showed the LDA results with 300-K thermal correction, and the results still differ considerably from the experimental results. From the static results, r^2SCAN and B3LYP are better choices for the brucite system than LDA and PBE, but LDA and PBE provide good lower and upper bounds for the key structure parameters. It should be noted that higher-level approaches, such as quantum Monte Carlo, can also be applied to benchmark DFT functionals [42].

B. Phonon stability

Phonon stability in brucite has been a debated topic in recent years. Treviño *et al.* [18] suggested that brucite needs to transform into a structure with an even lower symmetry $C2/m$ than $P\bar{3}$ or $P\bar{3}m1$. They ruled out $P\bar{3}$ and $P\bar{3}m1$ phases, as they display unstable temperature-dependent phonons at 300 K. According to their 300-K calculations using PBEsol, only $C2/m$ has stable phonons; at higher temperatures the other phases would also display stable phonons. However, in their comparison the q path for the $C2/m$ phase dispersion is nonequivalent from those in $P\bar{3}m1$ and $P\bar{3}$, which makes the comparison ambiguous. Also, their choice of PBEsol overestimates the volume of both $P\bar{3}m1$ and $P\bar{3}$ phases (see Table I).

Ab initio phonon calculations performed by Pillai *et al.* [15] suggested the $P\bar{3}m1$ symmetry would be the stable structure at ambient conditions using a nonempirical van der Waals functional (vdW-DF2) method. The discrepancy in their results suggests the importance of suitable exchange-correlation functionals for brucite. However, as shown in Table I, the vdW-DF2 results also overestimate the volume.

The success of r^2SCAN in describing the brucite structures suggests this functional should also be successful for phonon calculations. We calculate phonon dispersions for the $P\bar{3}m1$ and $P\bar{3}$ phases at a series of pressures. Figure 2 shows the phonon dispersions of $P\bar{3}$ brucite at ambient and elevated pressures. Detailed phonon dispersions for $P\bar{3}m1$ and $P\bar{3}$ brucite at several pressures can be found in the supplemental figures, Figs. S2 and S3 [37]. In contrast to previous results using other functionals [15,18], we find stable phonons for $P\bar{3}$ at all investigated pressures and unstable modes for $P\bar{3}m1$ (Figs. S2 and S3 [37]). This indicates that r^2SCAN, a functional that successfully describes H bonds, can also stabilize $P\bar{3}$ brucite at low and elevated pressures.

Although the consensus seems to be that $P\bar{3}$ is the stable brucite phase at higher pressure, here stable phonons of $P\bar{3}$ brucite are shown at elevated pressures.

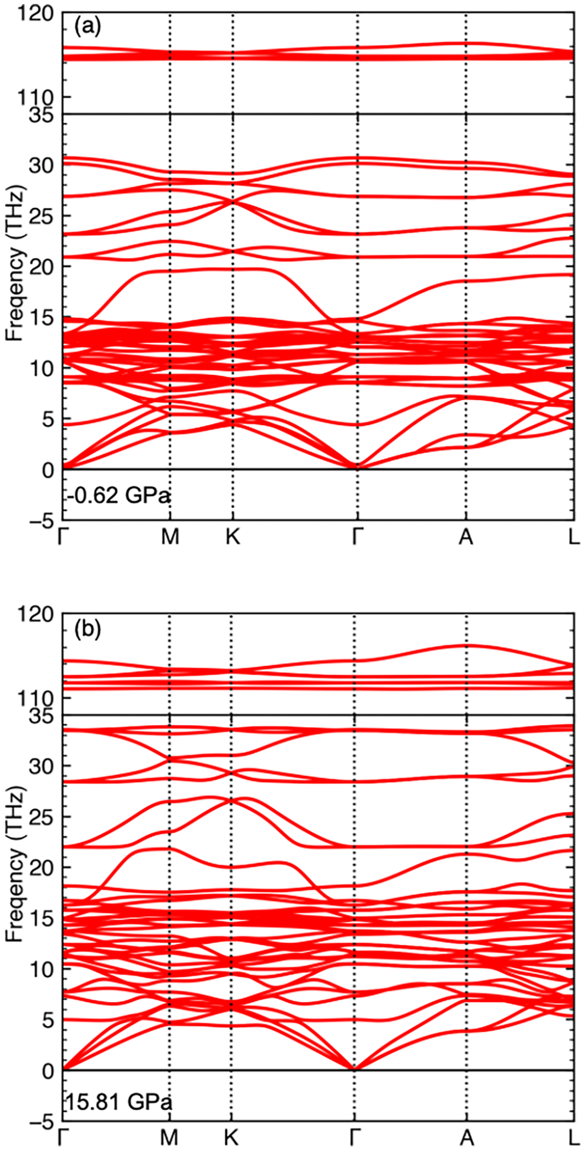

FIG. 2. Phonon spectra of $P\bar{3}$ brucite at (a) ambient and (b) elevated pressure. In both cases the phonon remains stable.

C. Equations of state

Figure 3 shows our calculated equations of state (EoS) using different exchange-correlation functionals and comparisons with measurements [11,12,43,45,48] and previous *ab initio* results [7,14,49]. The static compression curve is obtained by fitting the free energy vs volume with a third-order finite strain equation of state and then computing pressure as the free energy derivative with respect to volume. Our benchmark static LDA and PBE results agree well with previous calculations [7,14], showing ∼10% underestimation of volume by LDA and ∼5% overestimation with PBE compared to the measurements. r^2SCAN and B3LYP-D [49] results lie between LDA and PBE bounds and, at high pressures, lean close to PBE results. However, the semiempirical B3LYP-D [49] functional does not seem to account for the temperature effect as the others do, i.e., increase the volume uniformly from the static results, either using QHA or the Mie-Debye-Grüneisen model [7,14]. The B3LYP-D compression curve shape differs from the measurements also. Accounting for thermal effects, the B3LYP-D functional should overestimate the volume at higher pressures of geophysical significance. 300-K QHA r^2SCAN results are quite accurate between zero and 5 GPa, underscoring the necessity of including the finite-temperature effects in all calculations. Vibrational effects correct the volume by ∼5% at all pressures. The overall difference in volumes between 300 K QHA and measurements is less than 0.5 Å^3, less than the difference between measurements.

The stable r^2SCAN dispersions of $P\bar{3}$ brucite can be used to calculate the finite-temperature equation of state using the QHA method. Fitting P-V data to a third-order Birch-Murnaghan EoS gives $V_0 = 40.35$ Å^3, $B_0 = 49.35$ GPa, and $B' = 5.82$. Table II compares our EoS fitting parameters with previous measurements [11,12,43,46,48,50] and calculations [7,14,49]. Our V_0 is within the range of all measurements and agrees better with them than all previous calculations. Similarly, our B_0 and B' are also within the range of measurements. However, different measurements vary considerably,

TABLE II. Equation-of-state parameters compared to previous calculations and measurements. All experiments are at room temperature and ambient pressure, and all calculations are static unless otherwise stated.

Space group[a]	V_0 (Å^3)	B_0 (GPa)	B'	Method	Reference
$P\bar{3}m1$	40.87	54.30	4.70	X-ray diffraction	Fei and Mao (1993) [43]
$P\bar{3}m1$	40.20	47.00	4.70	Neutron diffraction	Parise (1994) [12]
$P\bar{3}m1$	40.99	39.00	7.60	Neutron diffraction	Catti (1995) [11]
$P\bar{3}m1$	40.85	42.00	5.70	X-ray diffraction	Duffy (1995) [44]
$P\bar{3}m1$	40.93	41.80	6.60	X-ray diffraction	Fukui (2003) [45]
$P\bar{3}m1$	41.10	35.80	8.90	Brillouin scattering	Jiang (2006) [46]
$P\bar{3}m1$	40.79	37.00	10.60	X-ray diffraction	Ma (2013) [48]
$P\bar{3}$	41.70	43.00	5.70	PBE	Mookherjee and Stixrude (2006) [14]
$P\bar{3}$	36.70	65.00	6.05	LDA	Mookherjee and Stixrude (2006) [14]
$P\bar{3}$	43.80	34.00	5.80	PBE 300 K	Mookherjee and Stixrude (2006) [14]
$P\bar{3}$	38.20	53.00	6.20	LDA 300 K	Mookherjee and Stixrude (2006) [14]
$P\bar{3}$	36.00	73.40	5.30	LDA	Ghaderi (2015) [7]
$P\bar{3}$	36.66	66.90	5.40	LDA 300 K	Ghaderi (2015) [7]
$P\bar{3}$	42.03	34.60	7.50	PBE	Ghaderi (2015) [7]
$P\bar{3}m1$	39.70	47.50	10.10	B3LYP-D	Ulian (2019) [49]
$P\bar{3}$	39.59	48.00	9.10	B3LYP-D	Ulian (2019) [49]
$P\bar{3}$	40.35	49.35	5.82	r^2SCAN 300 K	This work

[a] We keep the original convention from the references.

which might stem from the different pressure ranges these measurements used. Among all calculations, the fitting parameters from our r^2SCAN 300-K results agree best with measurements.

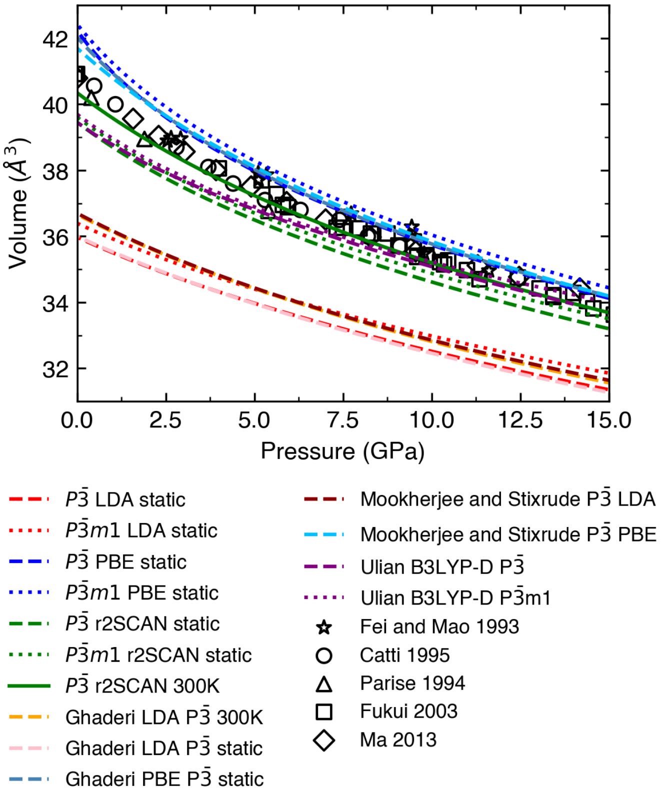

FIG. 3. Equation of state of $P\bar{3}$ and $P\bar{3}m1$ brucite phases calculated with different exchange-correlation functionals. Dashed lines: $P\bar{3}$; dotted lines: $P\bar{3}m1$. Different colors represent different exchange-correlation functionals (redlike: LDA; bluelike: PBE; green: r^2SCAN; purple: B3LYP).

D. Compression behavior

With a reliable EoS, we can investigate the structure evolution under pressure. Figure 4 shows the lattice parameters of optimized $P\bar{3}$ and $P\bar{3}m1$ brucite structures obtained with r^2SCAN compared to measurements [11,12,43,48] and previous B3LYP calculations [49]. Experimental results obtained using x-ray diffraction [43,48] and neutron diffraction [11,12] are consistent, except for the earliest one [43], which is slightly off. The discrepancy might be attributed to the nonhydrostaticity [48], as no pressure medium was used in Fei and Mao [43].

The 300-K structural parameters are obtained from V(P,300K) as determined by the QHA. Within this approximation's construct, crystal structure and vibrational spectrum depend on the volume alone. The extrinsic dependence of lattice parameters on temperature is indirect through the volume [51]. As long as there is a negligible temperature dependence of vibrational frequencies on the temperature at constant volume (anharmonicity), this is, in general, an excellent approximation for high-temperature structural parameters. The thermal stress tensor might deviate from the diagonal QHA pressure prediction for harmonic but elastically anisotropic crystals. In this case, an endless series of corrections is possible if one determines the thermoelastic coefficients iteratively [51,52]. This is usually a very small correction for harmonic crystals, and the first-order results provided here are adequate.

Compared to experiments, 300-K r^2SCAN calculations give the most consistent description of the lattice parameters and the anisotropic compression behavior described by the c/a ratio. Both $P\bar{3}$ and $P\bar{3}m1$ are more compressible along the c axis, as the structures have weak bonds along this direction.

Interlayer interaction is the result of the two forces: the attractive O · · · H—O forces and the repulsive H · · · H forces. The accurate description of both types of interactions plays an

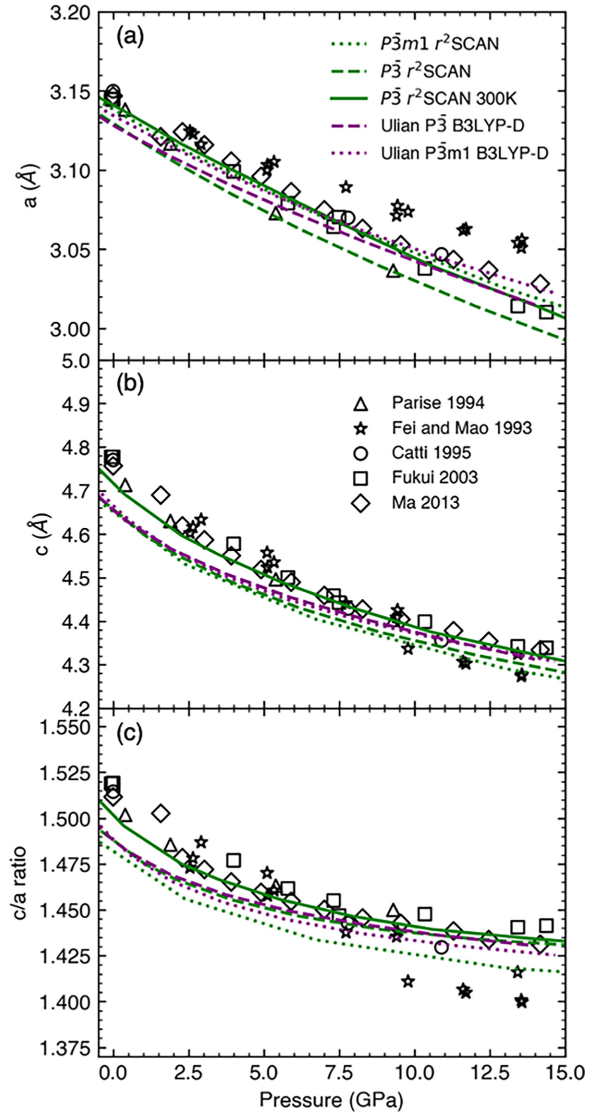

FIG. 4. Lattice parameters, (a) a, (b) c, and (c) c/a ratio in $P\bar{3}m1$ and $P\bar{3}$ brucite calculated with r^2SCAN. Dashed lines: $P\bar{3}$; dotted lines: $P\bar{3}m1$. Open black symbols represent experimental data [11,12,43,48]. Purple lines are results from previous calculations [49].

important role. Neutron-diffraction experiments can reveal the position of light elements (i.e., H) in the structure. However, whether to fit the structure using $P\bar{3}$ (H at $6i$) or $P\bar{3}m1$ (H at $2d$) symmetry has been a subjective choice. The assumed crystal symmetry influences the structural parameters shown in Fig. 5 extracted from neutron-diffraction spectra. For instance, proton positions in Ref. [11] were fitted to the $2d$-type site, while in Ref. [12] the $6i$-type site was used.

Figures 5(a) and 5(b) compare the H-bond length ($d_{\mathrm{O}\cdots H}$) and the bond angle ($\angle\mathrm{O}\cdots\mathrm{H—O}$) for $P\bar{3}$ and $P\bar{3}m1$ brucite structures obtained in the static and 300-K r^2SCAN calculation. They also show experimental measurements fitted to these two symmetries. We notice that the H-bond prediction agrees well with measurements in both phases, especially around 0 GPa. Notice that Refs. [12,47] report data on D instead of H, which could change $d_{\mathrm{O}\cdots\mathrm{H}}$ by as much as 0.1 Å in

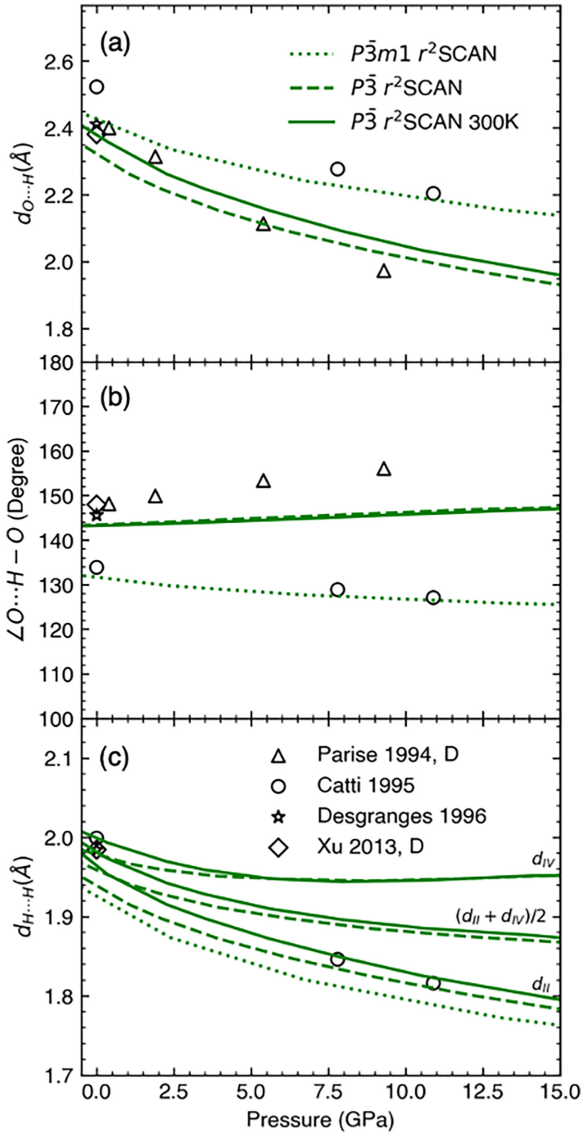

FIG. 5. Hydrogen bond length (a), angle (b), and H···H distances (c) in $P\bar{3}m1$ and $P\bar{3}$ brucite calculated using r^2SCAN and compared with experiments fitted to different symmetries [11,12,41,47]. There are two H···H distances distances in the $P\bar{3}$ structure and one only in the $P\bar{3}m1$ structure (see Fig. S4 [37]). Measurements marked with D represent $\mathrm{Mg(OD)_2}$.

a similar system also rich in H bonds, i.e., δ-AlOOH [53]. The H-bond angle [see Fig. 1(b)] in $P\bar{3}m1$ brucite is in excellent agreement with measurements [11]. Although the predicted H-bond angle of $P\bar{3}$ brucite deviates from measurements by 3%–5%, the pressure dependence of the H-bond behavior is correctly captured; for $P\bar{3}$ brucite, H bonds are shorter and the $\angle\mathrm{O}\cdots\mathrm{H—O}$ connecting two layers is closer to 180° compared to those in the $P\bar{3}m1$ phase. This suggests the H bond in $P\bar{3}$ structure is stronger than in the $P\bar{3}m1$ one. Under pressure, the H bond in $P\bar{3}$ shortens and strengthens with increasing H-bond angle. The opposite happens in the $P\bar{3}m1$ structure, i.e., this bond length decreases with decreasing angle, suggesting the H bond becomes less stable.

Figure 5(c) shows the H · · · H distances ($d_{\mathrm{H}\cdots H}$). As a result of lower symmetry and proton disorder, the $P\bar{3}$ model has two distinct H · · · H distances between layers, d_{II} and d_{IV} [14]. The visualization of d_{II}- and d_{IV}-type H · · · H is shown in the Supplemental Material in Fig. S4 [37]. They have distinct behavior under pressure: the d_{II} decreases monotonically with pressure, while the d_{IV} decreases at first and starts to increase at around 7.5 GPa. This behavior is consistent with previous PBE calculations by Mookherjee and Stixrude [14]. The average $d_{\mathrm{H}\cdots\mathrm{H}}$, or $\frac{1}{2}(d_{\mathrm{II}} + d_{\mathrm{IV}})$, agrees well with various measurements [11,12,41,47] at ambient pressures. The $d_{\mathrm{H}\cdots\mathrm{H}}$ in $P\bar{3}m1$ is much shorter than $P\bar{3}$, indicating a much stronger repulsion.

The stable phonon dispersion we get using r^2SCAN highlights the necessity of including nonlocal interactions in the brucite system. As shown in Fig. 5, the $P\bar{3}$ structure has a relatively stronger attractive H bond and weaker H · · · H repulsive interaction. The nonlocal interaction captured using r^2SCAN stabilizes the structure and yields stable phonons that would otherwise be unattainable using functionals without nonlocal interactions as captured by this meta-GGA.

E. Elasticity and velocity

With stable phonons from r^2SCAN calculations, we can compute the 300-K elastic properties and velocities of brucite with the SAM-Cij method [19,20]. The numbers of independent elastic tensor terms (c_{ij}) of $P\bar{3}m1$ and $P\bar{3}$ are slightly different [54]: they both have c_{11}, c_{12}, c_{13}, c_{14}, c_{33}, c_{44}, and $c_{66} = \frac{1}{2}(c_{11} - c_{12})$. In addition, $P\bar{3}$ has an independent nonzero c_{15}. Figure 6 shows the static and room-temperature elastic tensor components, c_{ij}, of $P\bar{3}m1$ and $P\bar{3}$ compared to measurements [46] and previous calculations [17,49]. Overall, for both $P\bar{3}m1$ and $P\bar{3}$, r^2SCAN results agree better with measurements than PBE [17] and B3LYP [49] calculations, except for c_{14}. However, considering the relatively small value of such an elastic constant, we can conclude that r^2SCAN performs well. Generally, the 300-K results give a correction that decreases the elastic constants and improves agreement with measurements. For c_{33} the correction can be as large as 30% at 0 GPa. Unfortunately, this type of high-temperature elastic constant calculation cannot be carried out for the $P\bar{3}m1$ structure because there are unstable phonons; nevertheless, the static results provide insight into the potential differences in elasticity between $P\bar{3}m1$ and $P\bar{3}$ brucite. Although the values are very similar, $P\bar{3}$ brucite agrees better with experiments than $P\bar{3}m1$. This coincides with our conclusion based on phonon stability.

The remaining deviation of the predicted elastic coefficients at 300 K might be due to the elastically anisotropic nature of the brucite structure [52]. Our r^2SCAN results on the P$\bar{3}$ structure suggest phonons are quite harmonic, contrary to predictions using the PBEsol functional [18]. Although anharmonicity in brucite deserves to be further investigated, it is beyond the scope of this paper.

Using elastic constants, we can calculate the Voigt-Reuss-Hill (VRH) average of the bulk and shear moduli. We compare our results with measurements [46] and previous calculations [49] [Fig. 7(a)]. Our r^2SCAN results agree better with measurements [46] than previous B3-D results [49]. In particular, our static results for the $P\bar{3}$ structure are closer to measurements than those for the $P\bar{3}m1$, and with thermal correction, the 300-K results agree even better at all pressures.

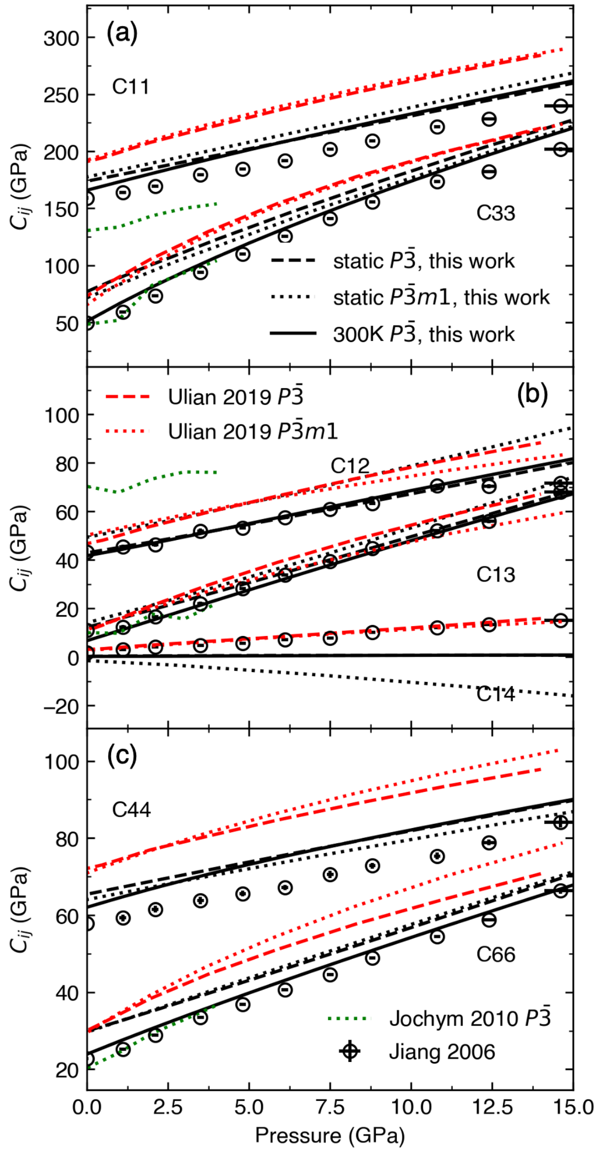

FIG. 6. Elastic tensor components (c_{ij}) vs pressure compared with single-crystal measurements [46] and calculations [17,49]. Results from Ref. [17] are calculated with PBE and results from Ref. [49] are using B3LYP.

The static and 300-K longitudinal and transverse velocity (V_P and V_S) and their pressure dependency are also plotted and compared with measurements [46] and previous calculations [49]. Note that the measured V_P and V_S are calculated from the data from the original paper [46] using the following relations: $V_P = \sqrt{(K_{\mathrm{VRH}} + \frac{4}{3}G_{\mathrm{VRH}})/\rho}$, $V_S = \sqrt{G_{\mathrm{VRH}}/\rho}$. In the low pressures, static and 300-K results differ the most. The agreement between our 300-K results and "measurements" is excellent, especially at 0 GPa, where they are almost identical. This result affirms that r^2SCAN can reproduce the measurements in such a system and that $P\bar{3}$ is the most suitable description of the brucite structure, even at

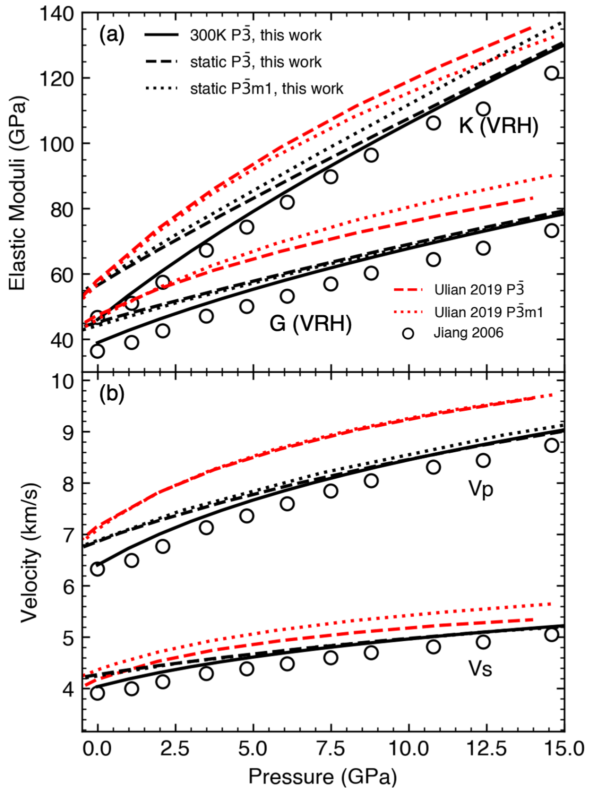

FIG. 7. (a) Elastic moduli and (b) seismic velocities vs pressure computed at static and 300-K condition compared to previous B3LYP calculation [49] and measurements [46].

ambient conditions. The V_P and V_S of $P\bar{3}$ at 300 K, 500 K, and 700 K are listed in Table SII [37] in the Supplemental Materials [37].

IV. CONCLUSIONS

Using *ab initio* calculations, we investigate the stability and elasticity of brucite. We tested several exchange-correlation functionals, including LDA, PBE, and r^2SCAN. The r^2SCAN functional outperforms other functionals (LDA, PBE, PBEsol, and B3LYP) in reproducing the 300-K compression curve and several key structure features involving H bonds when compared to measurements. The r^2SCAN functional also gives a dynamically stable $P\bar{3}$ brucite structure at relevant pressures. Such stable phonon dispersions combined with the QHA are used to compute 300-K elastic properties and acoustic velocities of $P\bar{3}$ brucite; results are in excellent agreement with the measurements. These successful calculations indicate that $P\bar{3}$ is the suitable space-group description of the brucite structure at ambient and elevated pressures. The success of the r^2SCAN functional for brucite suggests r^2SCAN should also be a suitable choice for studying other sheet hydrous minerals at relevant geophysical conditions of pressure and temperature.

ACKNOWLEDGMENTS

DOE Award No. DE-SC0019759 supported this work. We thank the anonymous reviewers for constructive comments on the manuscript. Calculations were performed on the Extreme Science and Engineering Discovery Environment (XSEDE) [55] supported by National Science Foundation (NSF) Grant No. 1548562 and the Advanced Cyberinfrastructure Coordination Ecosystem: Services & Support (ACCESS) program, which is supported by NSF Grants No. 2138259, No. 2138286, No. 2138307, No. 2137603, and No. 2138296 through allocation TG-DMR180081. Specifically, it used the *Bridges-2* system at the Pittsburgh Supercomputing Center (PSC), the *Anvil* system at Purdue University, the *Expanse* system at the San Diego Supercomputing Center (SDSC), and the *Delta* system at the National Center for Supercomputing Applications (NCSA).

[1] E. Ohtani, The role of water in earth's mantle, Natl. Sci. Rev. **7**, 224 (2020).

[2] M. Faccenda, Water in the slab: A trilogy, Tectonophysics **614**, 1 (2014).

[3] P. E. Van Keken, B. R. Hacker, E. M. Syracuse, and G. A. Abers, Subduction factory: 4. Depth-dependent flux of H_2O from subducting slabs worldwide, J. Geophys. Res. **116**, B01401 (2011).

[4] B. W. Evans, the serpentinite multisystem revisited: chrysotile is metastable, Int. Geol. Rev. **46**, 479 (2004).

[5] B. W. Evans, K. Hattori, and A. Baronnet, serpentinite: what, why, where? Elements **9**, 99 (2013).

[6] A. Hermann and M. Mookherjee, High-pressure phase of brucite stable at Earth's mantle transition zone and lower mantle conditions, Proc. Natl. Acad. Sci. USA **113**, 13971 (2016).

[7] N. Ghaderi, H. Zhang, and T. Sun, Relative stability and contrasting elastic properties of serpentine polymorphs from first-principles calculations, J. Geophys. Res. B: Solid Earth **120**, 4831 (2015).

[8] X. Deng, C. Luo, R. M. Wentzcovitch, G. A. Abers, and Z. Wu, Elastic anisotropy of lizardite at subduction zone conditions, Geophys. Res. Lett. **49**, e2022GL099712 (2022).

[9] F. Zigan and R. Rothbauer, Neutronenbeugungsmessungen am brucit, Neues Jahrbuch für Mineralogie, Monatshefte **1967**, 137 (1967).

[10] D. E. Partin, M. O'Keefe, and R. B. Von Dreele, Crystal structure and profile fitting of $Mg(OD)_2$ by time-of-flight neutron diffraction, J. Appl. Crystallogr. **27**, 581 (1994).

[11] M. Catti, G. Ferraris, S. Hull, and A. Pavese, Static compression and H disorder in brucite, $Mg(OH)_2$, to 11 GPa: A powder neutron diffraction study, Phys. Chem. Miner. **22**, 200 (1995).

[12] J. B. Parise, K. Leinenweber, D. J. Weidner, K. Tan, and R. B. Von Dreele, Pressure-induced H bonding: Neutron diffraction study of brucite, $Mg(OD)_2$, to 9.3 GPa, Am. Mineral. **79**, 193 (1994).

[13] S. Raugei, P. L. Silvestrelli, and M. Parrinello, Pressure-induced frustration and disorder in $Mg(OH)_2$ and $Ca(OH)_2$, Phys. Rev. Lett. **83**, 2222 (1999).

[14] M. Mookherjee and L. Stixrude, High-pressure proton disorder in brucite, Am. Mineral. **91**, 127 (2006).

[15] S. B. Pillai, B. Joseph, and P. K. Jha, Brucite ($Mg(OH)_2$) under small perturbation: A combined first principles and synchrotron

x-ray diffraction study, J. Phys. Chem. Solids **154**, 110078 (2021).

[16] A. Pishtshev, S. Z. Karazhanov, and M. Klopov, Materials properties of magnesium and calcium hydroxides from first-principles calculations, Comput. Mater. Sci. **95**, 693 (2014).

[17] P. T. Jochym, A. M. Oleś, K. Parlinski, J. Łażewski, P. Piekarz, and M. Sternik, Structure and elastic properties of $Mg(OH)_2$ from density functional theory, J. Phys.: Condens. Matter **22**, 445403 (2010).

[18] P. Treviño, A. C. Garcia-Castro, S. López-Moreno, A. Bautista-Hernández, E. Bobocioiu, B. Reynard, R. Caracas, and A. H. Romero, Anharmonic contribution to the stabilization of $Mg(OH)_2$ from first principles, Phys. Chem. Chem. Phys. **20**, 17799 (2018).

[19] Z. Wu and R. M. Wentzcovitch, Quasiharmonic thermal elasticity of crystals: An analytical approach, Phys. Rev. B **83**, 184115 (2011).

[20] C. Luo, X. Deng, W. Wang, G. Shukla, Z. Wu, and R. M. Wentzcovitch, cij: A Python code for quasiharmonic thermoelasticity, Comput. Phys. Commun. **267**, 108067 (2021).

[21] T. Sun, D.-B. Zhang, and R. M. Wentzcovitch, Dynamic stabilization of cubic CaSiO3 perovskite at high temperatures and pressures from *ab initio* molecular dynamics, Phys. Rev. B **89**, 094109 (2014).

[22] H. Wang, J. Zhuang, Z. Zhang, Q. Zhang, and R. M. Wentzcovitch, pgm: A Python package for free energy calculations within the phonon gas model, Comput. Phys. Commun. **291**, 108845 (2023).

[23] J. Zhuang, H. Wang, Q. Zhang, and R. M. Wentzcovitch, Thermodynamic properties of ϵ-Fe with thermal electronic excitation effects on vibrational spectra, Phys. Rev. B **103**, 144102 (2021).

[24] J. W. Furness, A. D. Kaplan, J. Ning, J. P. Perdew, and J. Sun, Accurate and numerically efficient r^2SCAN meta-generalized gradient approximation, J. Phys. Chem. Lett. **11**, 8208 (2020).

[25] J. P. Perdew, K. Burke, and M. Ernzerhof, Generalized gradient approximation made simple, Phys. Rev. Lett. **77**, 3865 (1996).

[26] J. P. Perdew and A. Zunger, Self-interaction correction to density-functional approximations for many-electron systems, Phys. Rev. B **23**, 5048 (1981).

[27] J. Sun, A. Ruzsinszky, and J. P. Perdew, Strongly constrained and appropriately normed semilocal density functional, Phys. Rev. Lett. **115**, 036402 (2015).

[28] M. Chen, H.-Y. Ko, R. C. Remsing, M. F. Calegari Andrade, B. Santra, Z. Sun, A. Selloni, R. Car, M. L. Klein, J. P. Perdew *et al.*, Ab initio theory and modeling of water, Proc. Natl. Acad. Sci. USA **114**, 10846 (2017).

[29] C. Luo, Y. Sun, and R. M. Wentzcovitch, Probing the state of hydrogen in δ-AlOOH at mantle conditions with machine learning potential, Phys. Rev. Res. **6**, 013292 (2024).

[30] T. Wan, C. Luo, Y. Sun, and R. M. Wentzcovitch, Thermoelastic properties of bridgmanite using deep-potential molecular dynamics, Phys. Rev. B **109**, 094101 (2024).

[31] J. Sun, R. C. Remsing, Y. Zhang, Z. Sun, A. Ruzsinszky, H. Peng, Z. Yang, A. Paul, U. Waghmare, X. Wu, M. L. Klein, and J. P. Perdew, Accurate first-principles structures and energies of diversely bonded systems from an efficient density functional, Nat. Chem. **8**, 831 (2016).

[32] M. Kothakonda, A. D. Kaplan, E. B. Isaacs, C. J. Bartel, J. W. Furness, J. Ning, C. Wolverton, J. P. Perdew, and J. Sun, Testing the r^2SCAN density functional for the thermodynamic stability of solids with and without a van der Waals correction, ACS Materials Au **3**, 102 (2023).

[33] J. Ning, J. W. Furness, and J. Sun, Reliable lattice dynamics from an efficient density functional approximation, Chem. Mater. **34**, 2562 (2022).

[34] P. E. Blöchl, Projector augmented-wave method, Phys. Rev. B **50**, 17953 (1994).

[35] G. Kresse and J. Furthmüller, Efficient iterative schemes for *ab initio* total-energy calculations using a plane-wave basis set, Phys. Rev. B **54**, 11169 (1996).

[36] A. Togo, L. Chaput, T. Tadano, and I. Tanaka, Implementation strategies in Phonopy and Phono3py, J. Phys.: Condens. Matter **35**, 353001 (2023).

[37] See Supplemental Material at http://link.aps.org/supplemental/10.1103/PhysRevB.109.214103 for Figs. S1–S4 and Tables SI and SII.

[38] T. Barron and M. Klein, Second-order elastic constants of a solid under stress, Proc. Phys. Soc. **85**, 523 (1965).

[39] T. Qin, Q. Zhang, R. M. Wentzcovitch, and K. Umemoto, qha: A Python package for quasiharmonic free energy calculation for multiconfiguration systems, Comput. Phys. Commun. **237**, 199 (2019).

[40] K. Momma and F. Izumi, Vesta 3 for three-dimensional visualization of crystal, volumetric and morphology data, J. Appl. Crystallogr. **44**, 1272 (2011).

[41] L. Desgranges, G. Calvarin, and G. Chevrier, Interlayer interactions in $M(OH)_2$: A neutron diffraction study of $Mg(OH)_2$, Acta Crystallogr. Sect. B: Struct. Sci. **52**, 82 (1996).

[42] S. Zhang, R. Paul, S.X. Hu, and M. A. Morales, Toward an accurate equation of state and B1-B2 phase boundary for magnesium oxide up to terapascal pressures and electron-volt temperatures, Phys. Rev. B **107**, 224109 (2023).

[43] Y. Fei and H.-K. Mao, Static compression of $Mg(OH)_2$ to 78 GPa at high temperature and constraints on the equation of state of fluid H_2O, J. Geophys. Res.: Solid Earth **98**, 11875 (1993).

[44] T. S. Duffy, J. Shu, H.-k. Mao, and R. J. Hemley, Single-crystal x-ray diffraction of brucite to 14 GPa, Phys. Chem. Miner. **22**, 277 (1995).

[45] H. Fukui, O. Ohtaka, T. Suzuki, and K. Funakoshi, Thermal expansion of $Mg(OH)_2$ brucite under high pressure and pressure dependence of entropy, Phys. Chem. Miner. **30**, 511 (2003).

[46] F. Jiang, S. Speziale, and T. S. Duffy, Single-crystal elasticity of brucite, $Mg(OH)_2$, to 15 GPa by Brillouin scattering, Am. Mineral. **91**, 1893 (2006).

[47] H. Xu, Y. Zhao, D. D. Hickmott, N. J. Lane, S. C. Vogel, J. Zhang, and L. L. Daemen, High-temperature neutron diffraction study of deuterated brucite, Phys. Chem. Miner. **40**, 799 (2013).

[48] M. Ma, W. Liu, Z. Chen, Z. Liu, and B. Li, Compression and structure of brucite to 31 GPa from synchrotron x-ray diffraction and infrared spectroscopy studies, Am. Mineral. **98**, 33 (2013).

[49] G. Ulian and G. Valdrè, Equation of state and second-order elastic constants of portlandite $Ca(OH)_2$ and brucite $Mg(OH)_2$, Phys. Chem. Miner. **46**, 101 (2019).

[50] T. S. Duffy, C. Meade, Y. Fei, H.-K. Mao, and R. J. Hemley, High-pressure phase transition in brucite, $Mg(OH)_2$, Am. Mineral. **80**, 222 (1995).

[51] P. Carrier, R. Wentzcovitch, and J. Tsuchiya, First-principles prediction of crystal structures at high temperatures using the quasiharmonic approximation, Phys. Rev. B **76**, 064116 (2007).

[52] P. Carrier, J. F. Justo, and R. M. Wentzcovitch, Quasiharmonic elastic constants corrected for deviatoric thermal stresses, Phys. Rev. B **78**, 144302 (2008).

[53] A. Sano-Furukawa, T. Hattori, K. Komatsu, H. Kagi, T. Nagai, J. J. Molaison, A. M. Dos Santos, and C. A. Tulk, Direct observation of symmetrization of hydrogen bond in δ-AlOOH under mantle conditions using neutron diffraction, Sci. Rep. **8**, 15520 (2018).

[54] K. Brugger, Pure modes for elastic waves in crystals, J. Appl. Phys. **36**, 759 (1965).

[55] J. Towns, T. Cockerill, M. Dahan, I. Foster, K. Gaither, A. Grimshaw, V. Hazlewood, S. Lathrop, D. Lifka, G. D. Peterson, R. Roskies, J. R. Scott, and N. Wilkins-Diehr, XSEDE: Accelerating scientific discovery, Comput. Sci. Eng. **16**, 62 (2014).